

Circumnuclear and infalling H I gas in a merging galaxy pair at $z = 0.123$

R. Srianand^{1*}, N. Gupta¹, E. Momjian², and M. Vivek³

¹ IUCAA, Postbag 4, Ganeshkhind, Pune 411007, India

² National Radio Astronomy Observatory, 1003 Lopezville Road, Socorro, NM 87801, USA

³ Department of Physics and Astronomy, University of Utah, Salt Lake City, UT 84112, USA

Accepted. Received; in original form

ABSTRACT

Using long-slit optical spectra obtained with the 2-m telescope at IUCAA Girawali Observatory, we show that the radio source J094221.98+062335.2 ($z = 0.123$) is associated with a galaxy pair undergoing a major merger. Its companion is a normal star-forming galaxy infalling with a velocity of 185 km s^{-1} at a projected separation of 4.8 kpc. Using the Westerbork Synthesis Radio Telescope (WSRT) and Giant Metrewave Radio Telescope (GMRT) we detect a strong H I 21-cm absorption at the systemic redshift of the radio galaxy with $N(\text{H I}) \sim 9 \times 10^{21} \text{ cm}^{-2}$ for an assumed spin-temperature of 100 K. Such a strong H I 21-cm absorption is rare and has been seen only in a few compact radio sources associated with similar merging galaxy pairs. Milliarcsecond resolution Very Long Baseline Array (VLBA) observations resolve the radio source into a compact symmetric object with the hotspot separation of 89 pc. The 21-cm absorption is detected in the VLBA spectra towards both the radio lobes albeit with a strong optical depth gradient. We show that the strong 21-cm absorption is consistent with it being arising from a clumpy circumnuclear disk/torus. We also detect two weaker absorption lines redshifted with respect to the radio source in the WSRT/GMRT spectrum. They probably represent cold (i.e. $T \leq 10^4 \text{ K}$) H I gas falling into the radio source. The presence of high concentration of H I gas in the circumnuclear regions and signature of infalling cold gas allows us to conjecture that the young radio source may have been triggered by the gas infall due to the ongoing merger.

Key words: quasars: active – quasars: absorption lines – quasars: individual: SDSS J094221.98+062335.2 – ISM: lines and bands

1 INTRODUCTION

It is now well recognised that active galactic nuclei (AGNs) play a vital role in the formation and evolution of their host galaxies (e.g. Silk & Rees 1998; Ferrarese & Merritt 2000; Fabian 2012). The so-called AGN feedback through winds from the accretion disk or by the relativistic radio jets can deposit large amounts of energy and momentum into the interstellar medium (ISM) of the host galaxy and its environment, and is often invoked in theoretical and numerical simulations to reproduce the observed properties of galaxies (e.g. Croton et al. 2006; Schawinski et al. 2006). At galactic scales, radio jets can regulate or prevent star formation i.e. provide the most commonly observed *negative* feedback by expelling or heating the gas. The radio jets can also trigger star formation i.e. provide *positive* feedback by shocking the

gas to high densities thereby accelerating the gas cooling processes (see e.g. van Breugel et al. 1986; Chambers et al. 1987; Daly 1990; Rejkuba et al. 2002; Gaibler et al. 2012).

While all these observational results confirm that the AGN feedback strongly influences the evolution of its host galaxy and the environment, the conditions prevailing in the host galaxy may also quench or trigger the AGN activity by altering the rate of accretion onto the central supermassive blackhole. One of the important questions in our understanding of the AGN is ‘What triggers the AGN activity?’. The galaxy-galaxy mergers represent one of the natural mechanisms to funnel large quantities of gas to the central ($< 1 \text{ pc}$) regions of galaxies and trigger the AGN. Several authors have found evidence for connection between the merger process and the AGN activity for both radio-loud and radio-quiet AGNs (e.g. Combes et al. 2009; Ellison et al. 2011; Ramos Almeida et al. 2012; Villar-Martín et al. 2012; Tadhunter et al. 2012; Khabiboulline et al. 2014). However,

* E-mail: anand@iucaa.ernet.in

there are also studies that find no relationship between the AGN activity and mergers (e.g. Cisternas et al. 2011; Schmitt 2001). In this context, it is of great interest to understand in detail the conditions that trigger AGN in galaxy mergers. It has been suggested that cold gas associated with the circumnuclear disk or torus may play a key role in fueling the AGN activity. Therefore, a natural way to test the connection between galaxy-galaxy mergers and the triggering of AGN activity will be to observe the properties of circumnuclear gas in AGN hosts associated with mergers.

For radio-loud AGNs, an interesting way of probing the properties of circumnuclear atomic gas, i.e. its distribution and kinematics, is via H I 21-cm absorption observations of the compact steep-spectrum (CSS) and gigahertz peaked-spectrum (GPS) sources¹. There have been several H I 21-cm absorption searches in samples of radio-loud AGNs involving these compact radio sources (e.g. Carilli et al. 1998; van Gorkom et al. 1989; Peck et al. 2000; Morganti et al. 2001; Vermeulen et al. 2003; Gupta et al. 2006; Chandola et al. 2011; Allison et al. 2012; Chandola et al. 2013; Geréb et al. 2015). High H I 21-cm absorption detection rate ($\sim 30\text{-}50\%$), young age ($<10^5$ yr) and the possibility of spatially resolved 21-cm absorption to trace the parsec scale distribution and kinematics of absorbing gas (see Table 1 of Araya et al. 2010, for a nice summary) makes these sources excellent candidates for understanding the triggering of AGN and its early stages of evolution.

As CSS and GPS sources are still embedded in their host galaxy ISM, they are also ideally suited for understanding the impact of radio mode feedback in the form of radio jet-ISM interaction (e.g. Gelderman & Whittle 1994; Axon et al. 2000; Gupta et al. 2005; Shih et al. 2013). In the H I 21-cm absorption studies, the AGN feedback due to CSS/GPS sources is revealed in the form of an excess of blue-shifted absorption lines with outflow velocities sometimes as high as ~ 1000 km s⁻¹ (Vermeulen et al. 2003; Morganti et al. 2005; Gupta et al. 2006; Chandola et al. 2011; Mahony et al. 2013; Morganti et al. 2013; Geréb et al. 2015). The incidences of redshifted or infalling gas clouds fuelling the AGN are rare (e.g. Araya et al. 2010; Maccagni et al. 2014).

In this paper, we report the detection and detailed analysis of the H I 21-cm absorption associated with a merging pair of galaxies at $z \sim 0.123$ having an angular separation of 2.2 arcsec. The absorption consists of a strong H I 21-cm absorption component at the systemic redshift of the radio galaxy and two well-detached, infalling weaker components.

This paper is structured as follows. In Section 2, we present details of optical and radio observations of the merging galaxy pair serendipitously discovered through our ongoing search for 21-cm absorption from quasar-galaxy pairs (Gupta et al. 2010, 2013)². In Section 3.1, we show that the

optical emission line ratios of the galaxy associated with the radio source, SDSS J094221.98+062335.2 (refer to as J0942+0623 from now on), are similar to those of AGNs whereas the optical spectrum of the other galaxy is consistent with a normal star forming galaxy. Besides a strong H I 21-cm absorption component at the systemic velocity of the radio-loud AGN, we also detect two redshifted absorption components representing a gas falling into the AGN. Section 3.2 focusses on deriving the properties of these H I absorption clouds from the arcsecond and milli-arcsecond scale spectroscopy. In Section 3.3, we discuss the relationship between the properties of H I 21-cm absorption and mergers using a sample of compact radio sources with 21-cm absorption measurements. Finally in Section 4, we summarize our results. Throughout this paper we use the cosmological model with $\Omega_\Lambda = 0.73$, $\Omega_M = 0.27$ and $H_0 = 71$ km s⁻¹Mpc⁻¹.

2 OBSERVATIONS AND DATA ANALYSIS

2.1 Optical: IGO spectroscopy

A single epoch optical spectrum of J094221.98+062335.2, observed on 27 February 2003, is available from the Sloan Digital Sky Survey (SDSS) archive. This spectrum covering a wavelength range of 3800-9200 Å was obtained with a fibre of diameter 3" centered at the position of the radio source and contains flux from both the galaxies. Therefore, to determine the redshifts and the nature of both the objects, we performed the long-slit spectroscopy of J0942+0623 using the IUCAA Faint Object Spectrograph (IFOSC) mounted on the 2-m IUCAA Girawali Observatory (IGO) telescope. We used Grisms 7 and 8 of IFOSC³ in combination with a long slit of 1.5" width. These settings provide a wavelength coverage of 3800–6840 Å and 5800–8350 Å, and a spectral resolution of 300 km s⁻¹ and 240 km s⁻¹, respectively. The Grism 8 data includes three 45 minutes exposures with the slit position angle, PA = 320° obtained on 25 February 2012 and three 45 minutes exposures with PA = 0° obtained on 26 April 2014. The Grism 7 data have one 45 minutes exposure with the PA = 0° obtained on 27 January 2011. The long slit orientations are shown in the *left* panel of Fig. 1. In the case of Grism 8, observations were carried out placing the object at different locations along the slit to take care of the fringing effects (see Vivek et al. 2009, for details).

For these data, the cleaning of raw frames and 1D spectral extraction were carried out following standard procedures in IRAF⁴. The two apertures that are shown overlaid on the 2-D spectra covering the H- α range in the *top-right* panel of Fig. 1 were chosen to extract 1D spectra of the objects, A (the host galaxy of the radio source) and B. The 1D spectra covering the H α and [N II] lines are shown in the *bottom-right* panel. The spectra covering H α , H β , [N II] and [O III] lines overlaid with Gaussian fits are shown in Fig 2.

¹ The CSS and GPS objects typically have sizes of <15 and 1 kpc, respectively and believed to be young ($<10^5$ yr) counterparts of the larger radio galaxies and QSOs (O'Dea 1998).

² Our sample of Quasar-Galaxy pairs at $z < 0.3$ is selected by cross-correlating galaxies detected in SDSS with radio loud AGNs in FIRST. There are 4 merging galaxy-galaxy pairs found. The 21-cm and optical observations of the remaining 3 sources are underway.

³ Details of the IGO/IFOSC grisms can be found at <http://www.iucaa.ernet.in/~itp/etc/ETC/help.html#grism>.

⁴ IRAF is distributed by the National Optical Astronomy Observatories, which are operated by the Association of Universities for Research in Astronomy, Inc., under cooperative agreement with the National Science Foundation.

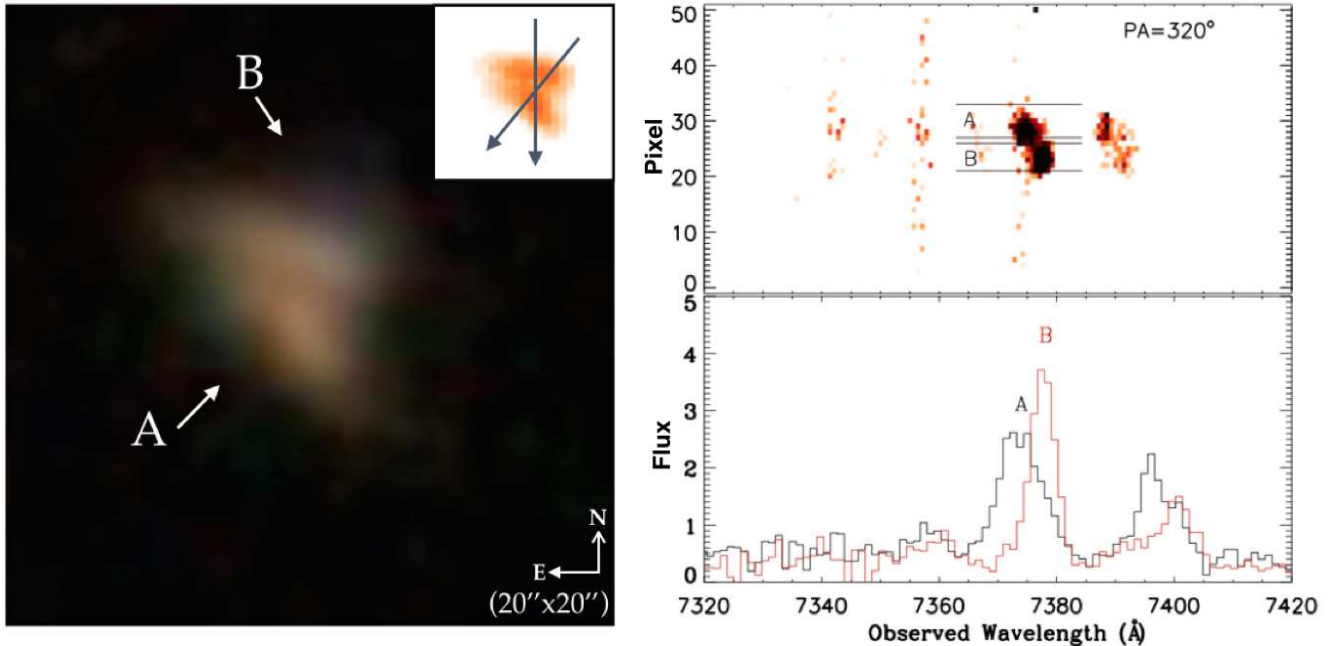


Figure 1. *Left:* SDSS colour composite image of the merging galaxy pair. The image, $20'' \times 20''$ in size, is centered at $\alpha_{J2000} = 09$ h 42 m 21.98 s, $\delta_{J2000} = 06$ d 23 m 35.2 s. In the inset, we show the r -band image. The positions of two slits used for the IGO spectroscopic observations are marked. *Top-right:* The 2D spectrum covering the wavelength range of $H\alpha$ emission for the exposures with slit PA = 320° . The two apertures used to extract the 1D spectra for the objects A and B are also marked. *Bottom-right:* One dimensional spectra corresponding to the two apertures showing the $H\alpha$ and [N II] emission lines.

It is clear from these figures that the redshift of object A is less than that of B. We measure $z_A = 0.1232 \pm 0.0001$ and $z_B = 0.1239 \pm 0.0001$. The angular separation between the objects is 2.2 arcsec. This corresponds to a projected separation of 4.8 kpc at the redshift of the radio source. The redshift difference measured corresponds to a velocity separation of $\sim 185 \text{ km s}^{-1}$. The angular and velocity separations found here are consistent with the definition of merging galaxies used by Ellison et al. (2011) to study the mergers in the SDSS database. In the following section, we study the line of sight distribution of the cold H I gas in this merging system using H I 21-cm absorption line as a tracer.

2.2 Radio: WSRT and GMRT spectroscopy

We observed J0942+0623 with Westerbork Synthesis Radio Telescope (WSRT) on 3 March 2011 to search for the associated 21-cm absorption. A total bandwidth of 10 MHz split into 2048 spectral channels was used to acquire the data in the dual polarization mode. This corresponds to a total bandwidth of $\sim 2400 \text{ km s}^{-1}$ and a channel width of $\sim 1.2 \text{ km s}^{-1}$ prior to Hanning smoothing. The bright calibrators 3C 286 and 3C 147 were used for flux density and bandpass calibration. The total on-source time, excluding calibration overheads, was ~ 9.8 hr. The data were analysed using AIPS⁵ following the standard procedures (Gupta et al. 2010). We detect 21-cm absorption spread over $\sim 300 \text{ km s}^{-1}$ in different components towards the radio

source that is, compact in our WSRT maps having a resolution of $180'' \times 14''$. The continuum normalised (stokes I) WSRT spectrum is shown in the *top* panel of Fig. 3. The measured continuum flux density is $\sim 113 \text{ mJy}$. The spectral resolution and the rms after applying Hanning smoothing are 2.4 km s^{-1} and $1.5 \text{ mJy beam}^{-1} \text{ channel}^{-1}$, respectively. The velocity scale, defined with respect to the $z_{\text{em}} = 0.1232$ corresponding to the systemic velocity of the radio source (i.e. object A), is also plotted on the *top* axis of the panel.

Redshifted 21-cm absorption line data are often affected by radio frequency interference (RFI). Our WSRT observations were no different in this regard. The data were carefully examined to flag and remove the RFI. However, certain frequency ranges were affected by the interference that was present on almost all the WSRT baselines for most of the times. These frequency ranges are marked as shaded regions in the *top* panel of Fig. 3, and affect the detectability of weak absorption features in the range: 1260-1263 MHz.

We observed the pair with Giant Metrewave Radio Telescope (GMRT) to confirm the weak H I absorption features detected in the WSRT spectrum. A bandwidth of 4 MHz split into 512 frequency channels was used to cover the frequency ranges: 1259-1263 MHz and 1263-1267 MHz on 16 and 17 July 2011, respectively. In both the observing runs, 3C 147 was observed for flux and bandpass calibration. In addition, nearby compact radio source 0925+003 was observed every ~ 45 minutes for phase calibration. In each observing run the total on-source time was ~ 3 hr. The data were analysed using AIPS following standard procedures. Relatively, the GMRT data were found to be much less affected by RFI. The flux density of the radio source J0942+0623 was found to be $\sim 116 \text{ mJy}$. Within the relative

⁵ See <http://www.aips.nrao.edu/index.shtml> for more information about AIPS

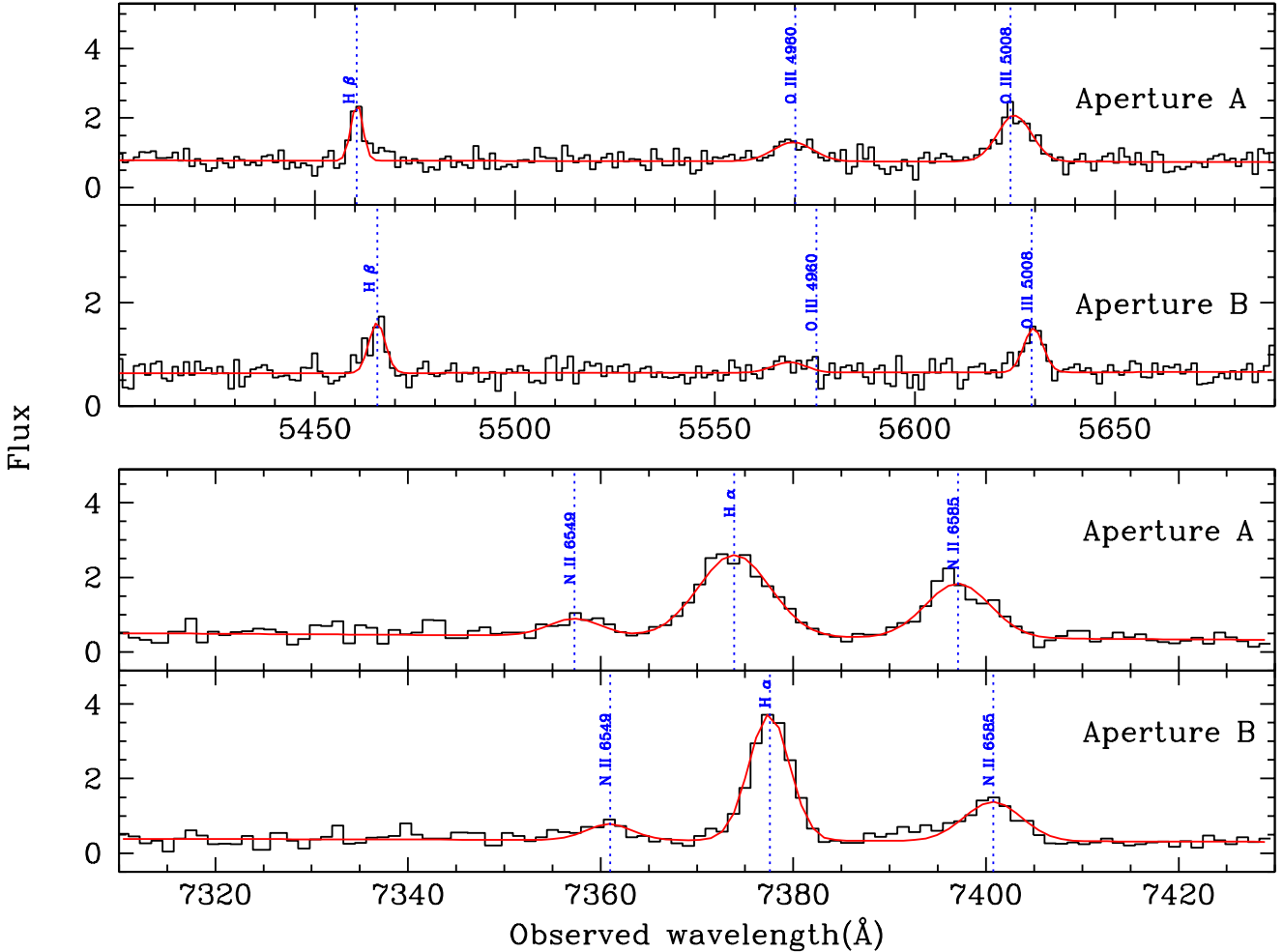


Figure 2. IGO spectra of object A and B together with Gaussian fits to the $H\alpha$, $H\beta$, $[N\ II]$ and $[O\ III]$ lines. It is clear that the emission lines are broader in the case of radio source (i.e. source A) which is at a lower redshift.

uncertainties, this is consistent with the WSRT measurement. The radio source is unresolved in the GMRT maps with a resolution of $\sim 3'' \times 2''$. The Stokes-I continuum normalised GMRT spectrum towards the radio source is shown in the *bottom* panel of Fig. 3. The spectral resolution is $\sim 1.9\text{ km s}^{-1}$ and the rms in the July 16 and 17 spectra are ~ 1.7 and $\sim 2.3\text{ mJy beam}^{-1}\text{ channel}^{-1}$, respectively. Similar to the WSRT spectrum, the frequency ranges affected by RFI in most of the data are marked as shaded region in Fig. 3.

The velocity shift due to the heliocentric motion of Earth between the WSRT and GMRT observing runs is 8 km s^{-1} . This allows us to distinguish the *real* 21-cm absorption components from the features due to RFI. A strong absorption component, labelled as ‘S’ in Fig. 3, and a weaker component, labelled as ‘W₁’, are detected in both the WSRT and GMRT spectrum at the observing frequency consistent with the heliocentric shift. Another component W₂, although very close to the RFI ‘spike’ in the GMRT spectrum, is consistently reproduced in both the spectra. None of the other weaker features in the frequency range 1260-1263 MHz

seen in the WSRT spectrum are reproduced in the GMRT spectrum and we consider these to be due to RFI.

The properties of absorption components S, W₁ and W₂ i.e. the absorption width, integrated 21-cm optical depth ($\int \tau dv$) and H I column density ($N(\text{H I})$) are summarized in Table 1. Note that the inferred large $N(\text{H I}) \sim 10^{22}\text{ cm}^{-2}$ is extremely rare in the samples of QSO sight lines tracing the ISM/halos of *normal* intervening galaxies via 21-cm, Mg II or damped Lyman- α (DLA) absorption (Gupta et al. 2010, 2012; Srianand et al. 2012; Noterdaeme et al. 2012). However, such $N(\text{H I})$ are more commonly associated with Gamma-ray bursts (e.g. Jakobsson et al. 2006), and galaxies at an impact parameter of a few kpc (Noterdaeme et al. 2014) i.e. the regions of high density close to the center of galaxy. Amongst the known 21-cm absorbers associated with AGNs such column densities (i.e. $\sim 10^{22}\text{ cm}^{-2}$) have been seen in a few cases i.e. J0111+3906 (also known as OC314), SDSS J150805.7+342323.3, UGC 6081, UGC 8387 and Mrk 273 (Carilli et al. 1998; Chandola et al. 2011; Darling et al. 2011; Geréb et al. 2015). It is clear from SDSS images that the host galaxies associated with

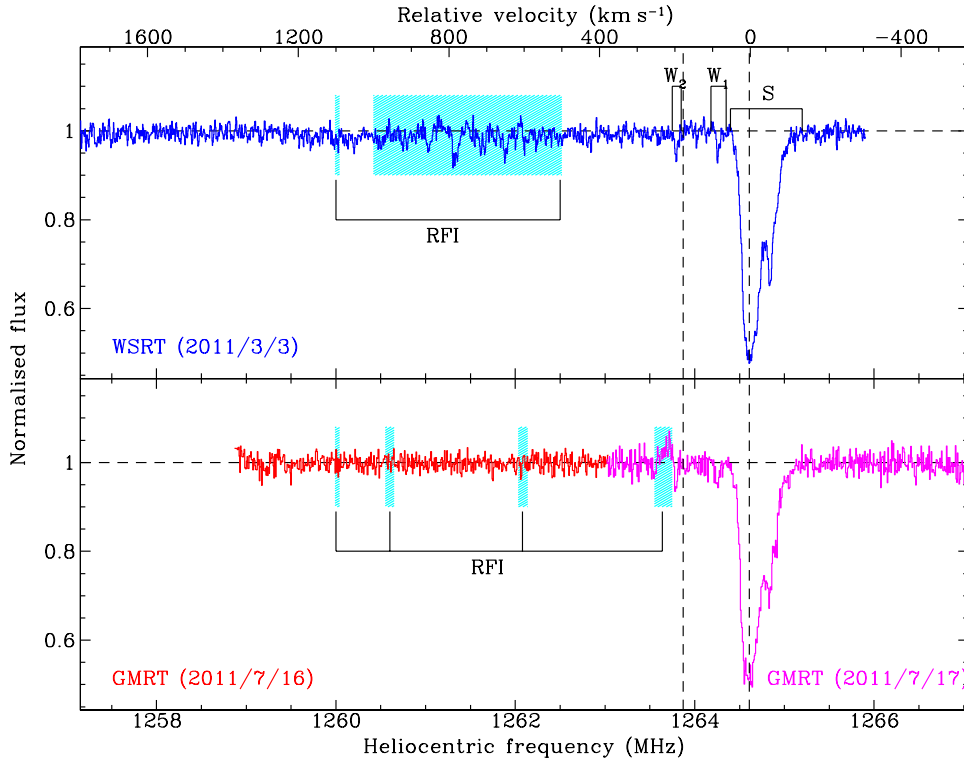


Figure 3. The WSRT (top) and GMRT (bottom) spectra of the radio source i.e. object A. The 21-cm absorption is clearly detected in a strong broad component (marked as S) at the systemic velocity of the radio source and two weak narrow absorption (marked as W_2 and W_1) with an infalling velocity in the range ~ 80 - 200 km s^{-1} . The velocity scale shown in the top panel is defined with respect to the systemic redshift $z = 0.1232$ of the radio source A. The vertical dashed lines correspond to redshifts of objects A and B.

Table 1. Properties of the 21-cm absorption components as measured from the WSRT spectrum

Component	Width [†] (km s^{-1})	$\int \tau(v)dv$ (km s^{-1})	$N(\text{H I})(100/T_s)(f_c/1.0)^{\ddagger}$ (10^{20} cm^{-2})
S	98	49.9 ± 0.4	91.0 ± 1.0
W_1	21	0.54 ± 0.09	0.99 ± 0.15
W_2	14	0.63 ± 0.07	1.15 ± 0.15

[†] Velocity width corresponding to 90% of the total $\int \tau dv$.

[‡] T_s = spin temperature; f_c = covering factor.

J1508+3423 at $z = 0.046$, UGC 6081 at $z = 0.036$, UGC 8387 at $z = 0.023$ and Mrk 273 at $z = 0.037$ are undergoing a major merger. In the case of higher redshift ($z = 0.6685$) source J0111+3906, the host galaxy shows asymmetric morphology (Stanghellini et al. 1998), possibly a signature of an ongoing or a recent merger. As galaxy mergers are expected to trigger the inflow of gas to the central regions of the galaxies, the large columns of H I gas associated with J0942+0623 and these five cases from the literature are caused by the ongoing mergers.

2.3 Radio: VLBA imaging and spectroscopy

The source J0942+0623 was observed with Very Long Baseline Array (VLBA) on 2012 June 15, 17 and 22. The goal of these observations was to perform the milliarcsecond resolution 1264 MHz continuum imaging and the redshifted H I 21-

cm absorption spectroscopy. The total observing time was 10 hr. The on-source time, excluding the telescope set-up time and calibration overheads, was ~ 6 hr. One 8 MHz-baseband channel pair covering the frequency range 1260.8-1268.8 MHz was used with right- and left-hand circular polarizations sampled at 2 bits. The data were correlated with 4000 spectral channels providing a spectral resolution of 2 kHz i.e. ~ 0.47 km s^{-1} . The correlator integration time was 2 s. We analysed the data following standard procedures in AIPS (see for example Momjian et al. 2002; Gupta et al. 2012). The continuum image of the radio source obtained by averaging absorption-free frequency channels is shown in Fig. 4. The rms in the image is $90 \mu\text{Jy beam}^{-1}$, and the spatial resolution i.e. the restoring beam is $0.01230'' \times 0.00436''$ with PA = -5.1° .

In the VLBA image, we recover $\sim 88\%$ of the total flux density detected in the GMRT and WSRT images. Most of the milliarcsecond scale flux is contained in the two components which are marked with ‘+’ in the Fig. 4. Hereafter, we refer to these as the northern and southern blobs, or VLBA-N and VLBA-S, respectively. The separation between the peaks of VLBA-N and VLBA-S is ~ 40 mas i.e. 89 pc at $z_g = 0.1232$. The overall radio morphology is similar to the Compact Symmetric Objects (CSOs) believed to be young ($< 10^5$ yr old) radio sources (e.g., Conway 2002). The peak and total flux densities of VLBA-N and VLBA-S are provided in Table 2. Both the blobs are spatially resolved and each can be fitted with two Gaussian components. We find that in each case more than 70% of the flux in the blob

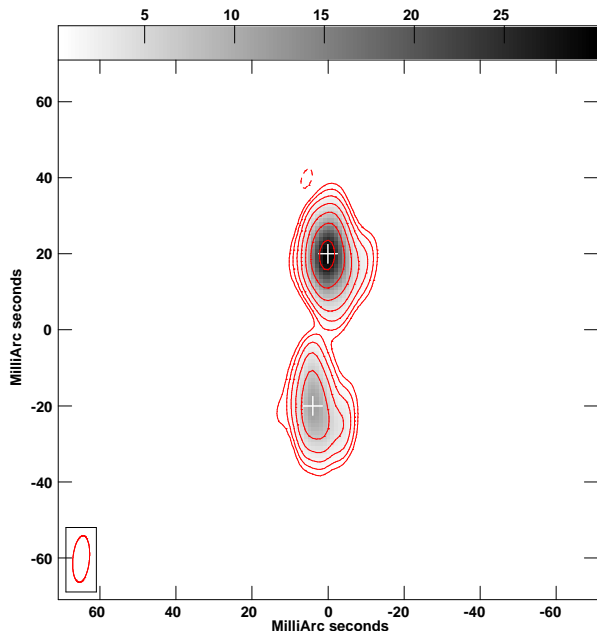


Figure 4. VLBA image of J0942+0623. The rms in the image is $90 \mu\text{Jy beam}^{-1}$. The contour levels are $4.0 \times 10^{-4} \times (-1, 1, 2, 4, 8, \dots) \text{Jy beam}^{-1}$. The gray scale range is: $0.4\text{--}30 \text{mJy beam}^{-1}$. The restoring beam (see text for details) is shown as an ellipse at the bottom left corner. The image centre is at RA = $09^{\text{h}} 42^{\text{m}} 21^{\text{s}}.9832$ and Dec. = $+06^{\circ} 23' 35''.1150$. The northern and southern peaks are marked with '+'. They are separated by $\sim 40 \text{mas}$ i.e. 89pc .

Table 2. Results of VLBA observations

Source component	Peak flux density (mJy beam^{-1})	Integrated flux density (mJy)	$\int \tau dv^\dagger$ (km s^{-1})
VLBA-N	31.0	68.9	33 ± 3
VLBA-S	11.9	31.4	118 ± 20

[†] Towards VLBA-N and VLBA-S peaks.

is contained in a Gaussian component coinciding with the peak with FWHM $< 10 \text{mas}$.

In the top panel of Fig. 5, we plot VLBA spectrum extracted towards the radio continuum detected in Fig. 4. The WSRT and integrated VLBA spectra match well within the uncertainties. This suggests that all the 21-cm absorption (except for W_1 and W_2 which are too weak to be detected in the VLBA spectrum) detected in the WSRT/GMRT data are recovered in the VLBA data, and no absorption is present towards the radio flux resolved out in the VLBA data. The 21-cm absorption spectra towards the VLBA-N and VLBA-S peaks are shown in the bottom two panels of Fig. 5. As the optical depth sensitivity falls off rapidly beyond the continuum peaks, instead of making spatially resolved optical depth maps, we will make detailed comparison of the spectra towards the VLBA-N and VLBA-S peaks with our GMRT and WSRT spectra. These results are presented in the next Section.

3 RESULTS AND DISCUSSION

In this section we present a detailed analysis of the optical and radio spectra and discuss the physical state of the merging galaxies and the H I gas producing the 21-cm absorption.

3.1 The merging galaxy pair: SDSS J0942+0623

We use Gaussian fits to the emission lines to measure the line parameters towards the objects A and B. For the object A, we measure the FWHM of the H α line to be 350km s^{-1} . We find $\log [[\text{O III}]\lambda 5007/\text{H}\beta] \sim 0.4$ and $\log [[\text{N II}]\lambda 6583/\text{H}\alpha] \sim -0.2$. These values are consistent with the source A being a narrow line AGN (see Fig 14.2 of Osterbrock & Ferland 2006). As per the definition of Kewley et al. (2006), the source A can be classified as a composite H II-AGN type galaxy. In comparison, the emission lines associated with the object B are typically narrow and barely resolved in the IGO spectrum. We find $\log [[\text{O III}]\lambda 5007/\text{H}\beta] \sim 0.0$ and $\log [[\text{N II}]\lambda 6583/\text{H}\alpha] \sim -0.4$. These values are consistent with what one expects from a H II region like object. Thus there are no signatures of any strong AGN activity in object B. Using the inferred H α luminosity we estimate the dust uncorrected starformation rate (using equations in Argence & Lamareille 2009) of $\sim 0.4 M_\odot \text{yr}^{-1}$. This suggests that there is no strong star-bursting activities in the central regions of object B. Thus, the objects A and B form an interacting pair of galaxies, with a separation of 4.8kpc , in which the former is a radio-loud narrow emission line AGN whereas the latter is a normal star-forming galaxy.

It is not unusual for an AGN to be associated with a host galaxy undergoing a merger. Several authors have found evidence for mergers to be associated with both radio-loud and radio-quiet AGNs (e.g. Combes et al. 2009; Ellison et al. 2011; Ramos Almeida et al. 2012; Villar-Martín et al. 2012; Tadhunter et al. 2012; Khabiboulline et al. 2014). In a few merging pairs, double AGNs have also been found (e.g. Evans et al. 2008; Tadhunter et al. 2012). Such systems are though extremely rare. In general, there could be several reasons for the lack of simultaneous AGN activities in both the merging galaxies like (i) intermittent supply of gas to the central regions or (ii) suppression of gas infall due to negative feedback caused by the nuclear starburst activity. In the case of object B, the lack of AGN activity is possibly due to the lack of cold gas supply to the central region.

3.2 Properties of the absorbing clouds

In this section, we first discuss the properties of component ‘S’ inferred from the arcsecond and milliarcsecond scale 21-cm absorption spectra. Following this we present the properties of well-detached narrow components W_1 and W_2 that are infalling with respect to the systemic redshift of the radio source. These features are detected only in the more sensitive GMRT and WSRT spectra.

3.2.1 The 21-cm absorption component: S

The 21-cm absorption component ‘S’ extends over the frequency range: $1264.4\text{--}1265.2 \text{MHz}$. The absorption profile exhibits substructure indicating multiple absorption compo-

nents. As is evident in Fig 3, the absorption profile is asymmetric with respect to the systemic redshift of the radio source with the blue wing extending upto -120 km s^{-1} and the red wing upto $+50 \text{ km s}^{-1}$. The 90% of the total optical depth is contained within $\sim 98 \text{ km s}^{-1}$ and the optical depth weighted centroid of the profile is almost (within $\sim 20 \text{ km s}^{-1}$) coincident with the systemic redshift of the radio source.

Recently, Geréb et al. (2015) used 21-cm absorption line shapes and systemic velocities for a sample of 32 absorbers to study the origin of the absorbing gas. They suggested that while the narrowest lines with “busy function” $\text{FWHM} < 100 \text{ km s}^{-1}$ detected close to the systemic velocities are likely to be produced by H I disks, the absorption with intermediate and large ($\text{FWHM} > 200 \text{ km s}^{-1}$) widths originate from H I disks with complex gas kinematics. Among the 21-cm detections in their sample, three sources (UGC 05101, UGC 8387 and Mrk 273) are associated with mergers, and all three exhibit extremely broad absorption lines spreading over $\sim 500\text{-}1000 \text{ km s}^{-1}$. Also, unlike J0942+0623 which is a CSO with an extent of 89 pc, the radio continuum associated with these mergers have complex morphology with much larger extents (Condon et al. 1990; Crawford et al. 1996; Carilli & Taylor 2000) suggesting that the absorbing gas is originating from gas with complex kinematics due to ongoing merger and interaction with the radio source.

The properties of component ‘S’ are akin to the class of H I absorbers with intermediate widths detected close to the systemic velocity. This suggests that the absorption originates from a circumnuclear disk having simple kinematics. However, the narrower H I absorption line in our case can be attributed to the compactness of the J0942+0623 which may be tracing only a small portion of H I gas velocity distribution.

To understand this further, we compare the WSRT/GMRT spectra with the VLBA spectra towards the peaks of VLBA-N and VLBA-S in Fig. 5. The differences in the optical depth are clearly seen towards these two sight lines separated by 89 pc (see bottom two panels of Fig. 5). The total integrated optical depth towards VLBA-S peak is higher by a factor of ~ 3.5 compared to that measured towards VLBA-N peak (see also Table 2).

The top two panels in Fig. 5 show the GMRT and WSRT spectra. First we check whether the individual absorbing gas detected towards the VLBA peaks cover all the radio emission from the corresponding VLBA component. For this we assume that the total flux seen in the WSRT/GMRT image is the sum of the fluxes of the two VLBA blobs. This allow us to predict the expected absorption profile in the WSRT/GMRT spectrum i.e.,

$$I_\nu = 0.314 \exp(-\tau_S(\nu)) + 0.686 \exp(-\tau_N(\nu)). \quad (1)$$

Here, I_ν is the normalised flux measured with WSRT/GMRT and τ_N and τ_S are the optical depth measured towards VLBA-N and VLBA-S respectively. The values 0.314 and 0.686 are the fractional radio flux contained in the VLBA-S and VLBA-N respectively.

The predicted absorption profile (solid smooth profile) using Eq. 1, is overlaid on the WSRT/GMRT spectra in the top two panels. It is clear that apart from the location where the peak absorption occurs towards VLBA-N, the predicted profile matches well with the observed one. This implies that

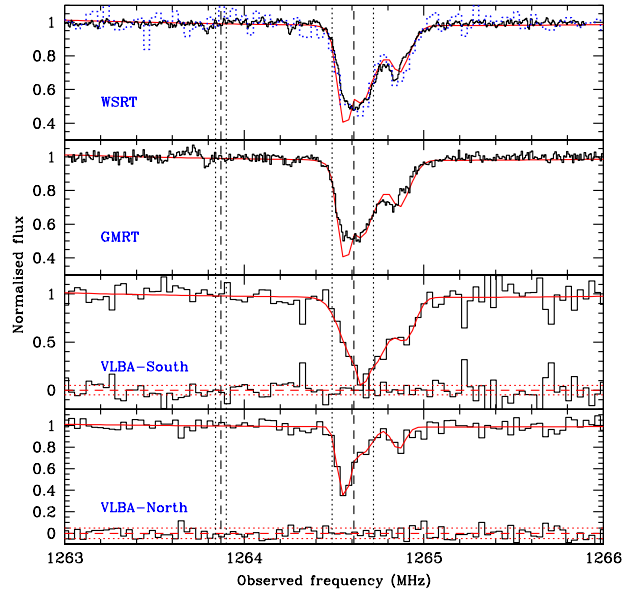


Figure 5. VLBA spectrum towards the northern (VLBA-N) and southern (VLBA-S) peaks marked in Fig. 4 are shown in bottom two panels. Multiple Gaussian fit to the 21-cm absorption is also overlaid. In the bottom of each of these panel residual flux resulting from the fits are compared to the rms flux measured in the line free regions. Top two panels show the GMRT and WSRT spectra. In these, we overlay the total VLBA spectrum *predicted* using spectra towards VLBA-N and VLBA-S peaks (see text for details). The vertical dashed and dotted lines mark the emission redshifts and associated errors respectively of object A and B. The integrated VLBA spectrum extracted towards the radio continuum detected in Fig. 4 is shown as dotted line in the top panel.

Table 3. Results of multiple gaussian fits to the 21-cm absorption detected towards the VLBA-N and VLBA-S peaks

ID	z_{abs}	τ_p	FWHM (km s^{-1})	$T_{\text{kin}}^{\text{max}}$ (K)	$\int \tau dv$ km s^{-1}
Fits for the profile towards VLBA-N					
N ₁	0.123245(1)	0.98(0.10)	17.04(1.27)	6350	17.8(0.3)
N ₂	0.123159(2)	0.29(0.03)	30.22(9.02)	21315	19.6(0.5)
N ₃	0.122975(5)	0.24(0.04)	19.70(3.59)	8490	5.0(0.2)
Fits for the profile towards VLBA-S					
S ₁	0.123154(1)	1.72(0.16)	9.36(1.33)	1916	17.2(0.5)
S ₂	0.123139(2)	1.56(0.05)	50.36(1.70)	55450	83.6(0.6)
S ₃	0.122940(4)	0.56(0.03)	26.38(2.13)	15210	15.4(0.2)

the projected extent of the gas responsible for most of the absorption is at least as big as the individual continuum emitting regions in the VLBA images (i.e $> 20 \text{ pc}$). However, the above noted inconsistency over a narrow velocity range could be due to the presence of absorption by compact gas with dimensions smaller than 20 pc.

Next we decompose the 21-cm H I absorption profiles towards VLBA-N and VLBA-S peaks using multiple Gaussians. We use these to examine if the properties of H I gas can be explained by a simple disk model. The fits are summarized in Table 3, and are plotted in the bottom two panels

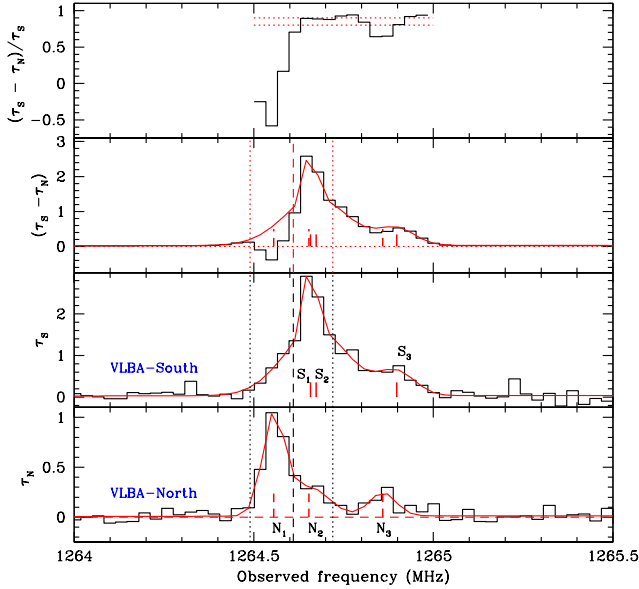


Figure 6. Measured H I 21-cm absorption optical depth towards the two VLBA components are shown in the bottom two panels. Optical depth difference is shown in the second panel from the top. The top panel shows the fractional optical depth excess towards the southern component. Central frequency of individual Gaussian components are marked. The vertical dotted dashed lines are as in Fig 5. In the top panel the dotted horizontal lines give the mean fractional variation in τ over the frequency range 1264.6 MHz and 1265 MHz.

of Fig. 6. Both the profiles are well fitted by three components. We label these components as N_1 to N_3 and S_1 to S_3 for VLBA-N and VLBA-S, respectively.

It is apparent that a Gaussian component at $z = 0.123245$ corresponding to N_1 is not required to fit the profile towards VLBA-S. This probably corresponds to the narrow component over-predicted by the VLBA profile noted earlier and arises from a distinct cloud that at best covers only the VLBA-N. Similarly the component S_1 is seen only towards VLBA-S. For an assumed spin temperature of 100 K, the $\log N(\text{H I})$ in both the cases is ~ 21.5 . If we assume the gas clouds to be spherical and covering only VLBA-N or VLBA-S then this will correspond to a gas density of $n_{\text{H}} \sim 50 \text{ cm}^{-3}$. The density will be higher if $T_S \gg 100 \text{ K}$ as expected in the vicinity of a strong radio continuum source. For typical jet advancement speeds of $\sim 0.1c$ observed in the case of compact radio sources, the ambient medium with clouds of such densities can confine the radio source (Taylor et al. 2000; Bicknell et al. 2003; Gugliucci et al. 2005; Jeyakumar et al. 2005). However, kinematically both N_1 and S_1 are consistent with the systemic velocity of the host galaxy within $\sim 10 \text{ km s}^{-1}$. This implies that these clouds are most likely associated with the circumnuclear disk or torus rather than the outflowing gas clouds interacting with the radio source.

The other two Gaussian components fitted to the spectrum towards VLBA-N and VLBA-S comprise $\sim 75\%$ of the total optical depth. These form a more coherent structure in opacity and kinematics that is consistent with a circumnuclear disk/torus like structure. The components N_2 and N_3

are within 10 km s^{-1} to the components S_2 and S_3 , respectively. This implies that there is no strong velocity gradient in the absorbing gas along the jet-axis i.e. the north-south direction.

In top two panels of Fig. 6, we plot the fractional optical depth, $(\frac{\tau_S - \tau_N}{\tau_S})$ and the difference optical depth, $(\tau_S - \tau_N)$ spectra. In the difference plot, we overlay the multiple Gaussian fit towards VLBA-S scaled by 0.85, the mean of $(\frac{\tau_S - \tau_N}{\tau_S})$ in the velocity range corresponding to S_2 and S_3 . Clearly the scaled τ_S fits match well with the difference spectra (i.e. $\tau_S - \tau_N$). This and the kinematical coincidence between N_2 (N_3) and S_2 (S_3) imply that these components cover both VLBA-N and VLBA-S albeit with an optical depth gradient from VLBA-N to VLBA-S i.e. over 89 pc. Following the circumnuclear disk model illustrated in the Fig. 5 of Orienti et al. (2006), the opacity gradient across the radio source can be explained by a combination of torus half-opening angle and, most importantly, the orientation of the line of sight such that the sight line towards VLBA-S traverses much longer path length through the disk (see also Gupta & Saikia 2006; Curran & Whiting 2010).

Thus, the VLBA spectroscopic observations are consistent with the absorption component ‘S’ originating from a clumpy circumnuclear disk (as seen by Momjian et al. 2003, in the case of NGC 7674).

3.2.2 The H I 21-cm absorption components: W_1 and W_2

We detect 21-cm absorption component W_1 and W_2 in the WSRT and GMRT spectrum. With respect to the radio source, these components have infall velocities of $\sim +85$ and $\sim +195 \text{ km s}^{-1}$ respectively. The widths corresponding to 90% of the total optical depth and the integrated optical depths of these components are summarized in Table 1. The narrow velocity spread seen is consistent with the infalling gas being clumpy rather than a smooth infalling distribution of gas where one expects to detect broad absorption lines. Typically, hotspot separation speeds of $\sim 0.1-0.5c$ have been observed for CSOs (e.g. Taylor et al. 2000). Adopting a value of 0.1c for J0942+0623 we obtain the kinematic age of ~ 1500 yrs. This recent AGN activity may have been triggered by the infalling gas whose signatures are still seen in the form of W_1 and W_2 .

The component W_1 at $z_{\text{abs}} = 0.1235$ is well represented by a single Gaussian component of FWHM of $6.4 \pm 1.0 \text{ km s}^{-1}$. This places a constraint on the kinetic temperature to be less than 900 K and correspondingly $\log N(\text{H I}) \leq 20.95^6$. Similarly, the component W_2 at $z_{\text{abs}} = 0.12393$ can also be fitted well with a single Gaussian component of FWHM of $11.5 \pm 1.5 \text{ km s}^{-1}$. This places a constraint on the kinetic temperature to be less than 2900 K and correspondingly $\log N(\text{H I}) \leq 21.46$. From Table 1 it is clear that for any realistic spin-temperature the inferred $N(\text{H I})$ will place the absorbing gas in the category of sub-DLAs or DLAs. The upper limit on the kinetic temperature derived for both these components are consistent with the infalling gas being cooler than what is expected (i.e. 10^4 K) for an

⁶ Here we assume that the line width provides the maximum allowed temperature and spin temperature is equal to the gas kinetic temperature.

intergalactic H I gas in photoionization equilibrium with the UV background radiation.

However, instead of being part of the infalling gas feeding the AGN, components W_1 and W_2 could simply be from (1) an intervening tidally disrupted gas or (2) the gas associated with objects A and B, respectively. This second possibility can be understood as following. As shown in Fig. 3, the blue wing of component ‘S’ extends upto $+120 \text{ km s}^{-1}$. The infall velocity ($+85 \text{ km s}^{-1}$) of W_1 is well within this range and it is possible that W_1 also originates from the same circumnuclear disk as ‘S’. Similarly, the component W_2 appears blueshifted with respect to object B by $\sim 10 \text{ km s}^{-1}$. But this is within the errors ($\sim 30 \text{ km s}^{-1}$) on the redshift of object B implying that W_2 may just be associated with object B.

3.3 Mergers and triggering of radio-loud AGN

It has already been established through various 21-cm absorption line surveys mentioned in Section 1 that detection rate of intrinsic 21-cm absorption amongst the compact radio sources is significantly higher ($\sim 50\%$) than in the extended sources (10-20%). This has been interpreted as the evidence of gas rich environment in these younger sources triggering the AGN activity. In this context, it is interesting to ask ‘what fraction of merging galaxies associated with compact radio sources are detected in H I 21-cm absorption detections?’.

This question can be addressed by considering the H I absorption study by Chandola et al. (2011). The study is based on 18 CSS and GPS sources drawn from the CORALZ sample (Compact Radio Sources at Low Redshift; Snellen et al. 2004). As all the sources in this study are at low- z ($z < 0.15$) and 16/18 are also covered in SDSS, it is possible to determine the merger fraction for these sources by visual inspection. We find that three CSS/GPS sources, namely, J1409+5216, J1508+3423 and J1718+5441 are associated with galaxy-galaxy mergers and exhibit morphological distortions and tidal features typically showed by such systems. All three are detected in 21-cm absorption with H I column densities in the range: $10^{21-22} \text{ cm}^{-2}$, which is at the higher end of column densities detected in their sample. This is also true for three mergers from the sample of Geréb et al. (2015) discussed in Section 3.2.1. All this further reinforces the point already mentioned in Section 2.2 that extremely high H I column densities ($\sim 10^{22} \text{ cm}^{-2}$), as seen in the case of J0942+0623, appear to be associated with galaxies undergoing major mergers. It is important to note that, in general at $N(\text{H I}) < 10^{22} \text{ cm}^{-2}$, one does see a mix of mergers and non-mergers, and the fraction of non-merging systems increases as the $N(\text{H I})$ cut-off is lowered. The major limitation at this point in quantifying this and drawing general conclusions is the unavailability of good quality optical imaging and spectroscopic data to reliably identify galaxy companions and mergers.

The galaxy-galaxy merger timescales ($\sim 10^9$ yrs) are substantially longer than the ages ($< 10^5$ yrs) of radio sources considered here. Therefore, while mergers/interactions may be responsible for funneling large volumes of gas to the centers of galaxies they may not be directly involved in triggering the AGN activity. This is concurrent with the recent findings that while AGN fraction may be higher amongst merg-

ing systems, mergers are not the dominant cause of AGN activity (see Ellison et al. 2011). The AGN activity may actually be triggered by local factors such as infall of gas due to disk instabilities. The 21-cm absorption components W_1 and W_2 detected towards J0942+0623 may be representing such gas clouds responsible for feeding the AGN. As noted in the previous section, the detection of infalling clumps in absorption is not sufficient to conclude that these are also responsible for fuelling the AGN. Additional constraints on gas geometry and kinematics, possibly from emission lines from ionized and molecular gas (e.g. Combes et al. 2014), are required to distinguish between various scenarios, and understand the role of mergers in triggering the AGN activity.

4 SUMMARY

Using long-slit optical spectroscopy, with the 2-m telescope at IGO, we show that SDSS J094221.98+062335.2 is a merging galaxy pair at $z \sim 0.123$ with a projected separation of 4.8 kpc. One of these i.e. object A has radio emission typical of CSOs. The measured emission line widths and line flux ratios are consistent with this object being a narrow line AGN. The other galaxy, i.e. object B, is found to be a normal star-forming galaxy and has an infall velocity of $\sim 185 \text{ km s}^{-1}$ with respect to the radio source.

We detect strong H I 21-cm absorption associated with the radio source using WSRT and GMRT. The H I column density, $N(\text{H I}) = 9.1 \times 10^{21} (T_s/100)(1.0/f_c) \text{ cm}^{-2}$ is one of the highest amongst the associated 21-cm absorbers. We find that some of the strong 21-cm absorbers with $N(\text{H I}) \sim 10^{22} \text{ cm}^{-2}$ reported in the literature are also associated with such major mergers. In the WSRT and GMRT spectra, we also detect two well-detached weaker 21-cm absorption components that are redshifted with respect to object A by $+85$ and $+195 \text{ km s}^{-1}$. These infalling absorptions could represent gas clouds fuelling the AGN. All this suggests a possibility that the large volumes of H I gas detected in these objects are caused by merger-driven inflows of gas that *could probably be* responsible for triggering and fuelling the central AGN.

At milliarcsecond scale resolution, the radio source is resolved into a CSO like morphology with 88% of the arc-second scale flux in two dominant continuum components separated by 89 pc. The 21-cm absorption at velocities corresponding to the strong 21-cm absorption component detected in the WSRT and GMRT spectra is detected towards both the continuum components albeit with an opacity gradient of as much as 3 over 89 pc. The VLBA spectra are not sensitive enough to detect the weaker redshifted absorption components mentioned above. Comparing the VLBA with the WSRT/GMRT spectra we find that the properties of strong 21-cm absorption component are consistent with the absorption arising from a circumnuclear disk/torus associated with object A. In this model, the opacity gradient across the radio source can be explained by a combination of torus half-opening angle and, most importantly, the orientation of the line of sight such that the sight line towards the southern VLBA component traverses much longer path length through the disk.

The available data does not rule out the possibility that

instead of originating from gas inflow feeding the AGN, the absorptions at +85 and 195 km s⁻¹, could simply be from (1) intervening tidally disrupted gas or (2) gas associated with the ISMs of objects A and B, respectively. Additional constraints on gas geometry and kinematics are required to distinguish between various scenarios and understand the role of mergers in triggering the AGN activity.

5 ACKNOWLEDGEMENTS

We acknowledge the use of SDSS images and spectra from the archive (<http://www.sdss.org/>). We thank IGO, GMRT, VLBA and WSRT staff for their support during the observations. Special thanks to Dr. Vijay mohan for service observations at IGO. We also thank the referee Prof. Morganti for useful suggestions. The VLBA is run by National Radio Astronomy Observatory. The VLBA data were correlated using NRAO implementation of the DiFX software correlator (Deller et al. 2011) that was developed as part of the Australian Major National Research facilities Programme and operated under license. The National Radio Astronomy Observatory is a facility of the National Science Foundation operated under cooperative agreement by Associated Universities, Inc. GMRT is run by the National Centre for Radio Astrophysics of the Tata Institute of Fundamental Research.

REFERENCES

- Allison J. R., Curran S. J., Emonts B. H. C., Geréb K., Mahony E. K., Reeves S., Sadler E. M., Tanna A., Whiting M. T., Zwaan M. A., 2012, *MNRAS*, 423, 2601
- Araya E. D., Rodríguez C., Pihlström Y., Taylor G. B., Tremblay S., Vermeulen R. C., 2010, *AJ*, 139, 17
- Argence B., Lamareille F., 2009, *A&A*, 495, 759
- Axon D. J., Capetti A., Fanti R., Morganti R., Robinson A., Spencer R., 2000, *AJ*, 120, 2284
- Bicknell G. V., Saxton C. J., Sutherland R. S., 2003, *PASA*, 20, 102
- Carilli C. L., Menten K. M., Reid M. J., Rupen M. P., Yun M. S., 1998, *ApJ*, 494, 175
- Carilli C. L., Taylor G. B., 2000, *ApJ*, 532, L95
- Chambers K. C., Miley G. K., van Breugel W., 1987, *Nature*, 329, 604
- Chandola Y., Gupta N., Saikia D. J., 2013, *MNRAS*, 429, 2380
- Chandola Y., Sirothia S. K., Saikia D. J., 2011, *MNRAS*, 418, 1787
- Cisternas M., Jahnke K., Inskip K. J., Kartaltepe J., Koekemoer A. M., Lisker T., Robaina A. R., Scodreggio M., Sheth K., Trump J. R., Andrae R., Miyaji T., Lusso E., Brusa M., Capak P., Cappelluti N., Civano F., Ilbert O., Impey C. D., Leauthaud A., Lilly S. J., Salvato M., Scoville N. Z., Taniguchi Y., 2011, *ApJ*, 726, 57
- Combes F., Baker A. J., Schinnerer E., García-Burillo S., Hunt L. K., Boone F., Eckart A., Neri R., Tacconi L. J., 2009, *A&A*, 503, 73
- Combes F., García-Burillo S., Casasola V., Hunt L. K., Krips M., Baker A. J., Boone F., Eckart A., Marquez I., Neri R., Schinnerer E., Tacconi L. J., 2014, *A&A*, 565, A97
- Condon J. J., Helou G., Sanders D. B., Soifer B. T., 1990, *ApJS*, 73, 359
- Conway J. E., 2002, *New A Rev.*, 46, 263
- Crawford T., Marr J., Partridge B., Strauss M. A., 1996, *ApJ*, 460, 225
- Croton D. J., Springel V., White S. D. M., De Lucia G., Frenk C. S., Gao L., Jenkins A., Kauffmann G., Navarro J. F., Yoshida N., 2006, *MNRAS*, 365, 11
- Curran S. J., Whiting M. T., 2010, *ApJ*, 712, 303
- Daly R. A., 1990, *ApJ*, 355, 416
- Darling J., Macdonald E. P., Haynes M. P., Giovanelli R., 2011, *ApJ*, 742, 60
- Deller A. T., Brisken W. F., Phillips C. J., Morgan J., Alef W., Cappallo R., Middelberg E., Romney J., Rottmann H., Tingay S. J., Wayth R., 2011, *PASP*, 123, 275
- Ellison S. L., Patton D. R., Mendel J. T., Scudder J. M., 2011, *MNRAS*, 418, 2043
- Evans D. A., Fong W.-F., Hardcastle M. J., Kraft R. P., Lee J. C., Worrall D. M., Birkinshaw M., Croston J. H., Muxlow T. W. B., 2008, *ApJ*, 675, 1057
- Fabian A. C., 2012, *ARA&A*, 50, 455
- Ferrarese L., Merritt D., 2000, *ApJ*, 539, L9
- Gaibler V., Khochfar S., Krause M., Silk J., 2012, *MNRAS*, 425, 438
- Gelderman R., Whittle M., 1994, *ApJS*, 91, 491
- Geréb K., Maccagni F. M., Morganti R., Oosterloo T. A., 2015, *A&A*, 575, A44
- Gugliucci N. E., Taylor G. B., Peck A. B., Giroletti M., 2005, *ApJ*, 622, 136
- Gupta N., Saikia D. J., 2006, *MNRAS*, 370, 738
- Gupta N., Salter C. J., Saikia D. J., Ghosh T., Jeyakumar S., 2006, *MNRAS*, 373, 972
- Gupta N., Srianand R., Bowen D. V., York D. G., Wadadekar Y., 2010, *MNRAS*, 408, 849
- Gupta N., Srianand R., Noterdaeme P., Petitjean P., Muzahid S., 2013, *A&A*, 558, A84
- Gupta N., Srianand R., Petitjean P., Bergeron J., Noterdaeme P., Muzahid S., 2012, *A&A*, 544, A21
- Gupta N., Srianand R., Saikia D. J., 2005, *MNRAS*, 361, 451
- Jakobsson P., Fynbo J. P. U., Ledoux C., Vreeswijk P., Kann D. A., Hjorth J., Priddey R. S., Tanvir N. R., Reichart D., Gorosabel J., Klose S., Watson D., Sollerman J., Fruchter A. S., de Ugarte Postigo A., Wiersema K., Björnsson G., Chapman R., Thöne C. C., Pedersen K., Jensen B. L., 2006, *A&A*, 460, L13
- Jeyakumar S., Wiita P. J., Saikia D. J., Hooda J. S., 2005, *A&A*, 432, 823
- Kewley L. J., Groves B., Kauffmann G., Heckman T., 2006, *MNRAS*, 372, 961
- Khajiboulline E. T., Steinhardt C. L., Silverman J. D., Ellison S. L., Mendel J. T., Patton D. R., 2014, *ApJ*, 795, 62
- Maccagni F. M., Morganti R., Oosterloo T. A., Mahony E. K., 2014, *A&A*, 571, A67
- Mahony E. K., Morganti R., Emonts B. H. C., Oosterloo T. A., Tadhunter C., 2013, *MNRAS*, 435, L58
- Momjian E., Romney J. D., Carilli C. L., Troland T. H., 2003, *ApJ*, 597, 809
- Momjian E., Romney J. D., Troland T. H., 2002, *ApJ*, 566,

- 195
- Morganti R., Fogasy J., Paragi Z., Oosterloo T., Orienti M., 2013, *Science*, 341, 1082
- Morganti R., Oosterloo T. A., Tadhunter C. N., van Moorsel G., Killeen N., Wills K. A., 2001, *MNRAS*, 323, 331
- Morganti R., Tadhunter C. N., Oosterloo T. A., 2005, *A&A*, 444, L9
- Noterdaeme P., Petitjean P., Carithers W. C., Pâris I., Font-Ribera A., Bailey S., Aubourg E., Bizyaev D., Ebelke G., Finley H., Ge J., Malanushenko E., Malanushenko V., Miralda-Escudé J., Myers A. D., Oravetz D., Pan K., Pieri M. M., Ross N. P., Schneider D. P., Simmons A., York D. G., 2012, *A&A*, 547, L1
- Noterdaeme P., Petitjean P., Pâris I., Cai Z., Finley H., Ge J., Pieri M. M., York D. G., 2014, *A&A*, 566, A24
- O’Dea C. P., 1998, *PASP*, 110, 493
- Orienti M., Morganti R., Dallacasa D., 2006, *A&A*, 457, 531
- Osterbrock D. E., Ferland G. J., 2006, *Astrophysics of gaseous nebulae and active galactic nuclei*
- Peck A. B., Taylor G. B., Fassnacht C. D., Readhead A. C. S., Vermeulen R. C., 2000, *ApJ*, 534, 104
- Ramos Almeida C., Bessiere P. S., Tadhunter C. N., Pérez-González P. G., Barro G., Inskip K. J., Morganti R., Holt J., Dicken D., 2012, *MNRAS*, 419, 687
- Rejkuba M., Minniti D., Courbin F., Silva D. R., 2002, *ApJ*, 564, 688
- Schawinski K., Khochfar S., Kaviraj S., Yi S. K., Boselli A., Barlow T., Conrow T., Forster K., Friedman P. G., Martin D. C., Morrissey P., Neff S., Schiminovich D., Seibert M., Small T., Wyder T. K., Bianchi L., Donas J., Heckman T., Lee Y.-W., Madore B., Milliard B., Rich R. M., Szalay A., 2006, *Nature*, 442, 888
- Schmitt H. R., 2001, *AJ*, 122, 2243
- Shih H.-Y., Stockton A., Kewley L., 2013, *ApJ*, 772, 138
- Silk J., Rees M. J., 1998, *A&A*, 331, L1
- Snellen I. A. G., Mack K.-H., Schilizzi R. T., Tschager W., 2004, *MNRAS*, 348, 227
- Srianand R., Gupta N., Petitjean P., Noterdaeme P., Ledoux C., Salter C. J., Saikia D. J., 2012, *MNRAS*, 421, 651
- Stanghellini C., O’Dea C. P., Dallacasa D., Baum S. A., Fanti R., Fanti C., 1998, *A&AS*, 131, 303
- Tadhunter C. N., Ramos Almeida C., Morganti R., Holt J., Rose M., Dicken D., Inskip K., 2012, *MNRAS*, 427, 1603
- Taylor G. B., Marr J. M., Pearson T. J., Readhead A. C. S., 2000, *ApJ*, 541, 112
- van Breugel W. J. M., Heckman T. M., Miley G. K., Filippenko A. V., 1986, *ApJ*, 311, 58
- van Gorkom J. H., Knapp G. R., Ekers R. D., Ekers D. D., Laing R. A., Polk K. S., 1989, *AJ*, 97, 708
- Vermeulen R. C., Pihlström Y. M., Tschager W., de Vries W. H., Conway J. E., Barthel P. D., Baum S. A., Braun R., Bremer M. N., Miley G. K., O’Dea C. P., Röttgering H. J. A., Schilizzi R. T., Snellen I. A. G., Taylor G. B., 2003, *A&A*, 404, 861
- Villar-Martín M., Cabrera Lavers A., Bessiere P., Tadhunter C., Rose M., de Breuck C., 2012, *MNRAS*, 423, 80
- Vivek M., Srianand R., Noterdaeme P., Mohan V., Kuriakosde V. C., 2009, *MNRAS*, 400, L6